Unraveling the Cobalt Oxidation State at the Surface of Epitaxial Cobalt Oxide Films during the Oxygen Evolution Reaction by Operando X-ray Absorption Spectroscopy/Surface X-ray Diffraction

Mathilde Bouvier, Ivan Pacheco Bubi, Tim Wiegmann, Canrong Qiu, Philippe Allongue, Olaf Magnussen, Fouad Maroun

Unravelling the cobalt oxidation state at the surface of epitaxial cobalt oxide films during oxygen evolution reaction by operando XAS / SXRD

Mathilde Bouvier [a], Ivan Pacheco Bubi [a], Tim Wiegmann [b], Canrong Qiu [b], Philippe Allongue [a*], Olaf M. Magnussen [b,*] Fouad Maroun [a,*]

[a] *Laboratoire de Physique de la Matière Condensée (PMC), CNRS, Ecole Polytechnique, Institut Polytechnique de Paris, F-91120 Palaiseau, France*

[b] *Institut für Experimentelle und Angewandte Physik, Christian-Albrechts-Universität zu Kiel, D-24098 Kiel, Germany*

** corresponding authors:*
fouad.maroun@polytechnique.edu, magnussen@physik.uni-kiel.de, philippe.allongue@polytechnique.edu

Abstract

Better understanding of the oxygen evolution reaction on cobalt oxides requires insights into the oxide-solution interface structure and composition under reaction conditions. We here present operando studies of electrodeposited epitaxial thin films with planar surface morphology that couple X-ray absorption spectroscopy, surface X-ray diffraction, and electrochemical measurements. This enabled us to disentangle bulk and surface contributions of the XAS signal and to correlate the cobalt oxidation state with the surface structure of cobalt oxide films. In the case of Co_3O_4(111) films, we show a one-to-one correlation between the Co oxidation state increase in the pre-OER potential range and the potential-dependent thickness of the reversibly formed amorphous layer on the oxide surface. From this correlation, we conclude that this amorphous layer is exclusively composed of Co^{3+}. In the case of CoOOH(001) films, we show that no such surface amorphization takes place and that the small oxidation state change with potential may be attributed to the progressive deprotonation of the surface Co-OH groups. For both oxides, the amount of Co^{4+} remains below the detection limit.

Keywords: oxygen evolution reaction, cobalt oxide, epitaxial films, operando X ray absorption spectroscopy, operando X ray diffraction, cobalt oxidation state, skin layer.

1. Introduction

Electrochemical water splitting into oxygen and hydrogen is a promising route for renewable energies conversion and storage. The kinetics of the oxygen evolution reaction (OER) is one of the main limiting factors of this technology. The development of efficient and economically viable catalysts for OER is thus essential for large scale development of this energy conversion [1]. A large number of studies focused on earth-abundant transition metal oxides which have interesting catalytic properties and high stability in alkaline medium [2-5]. Among those, cobalt oxides have been the subject of numerous experimental [6-27] and computational [16, 23, 28-32] studies.

In most of the OER mechanisms on Co oxides, the oxidation state of Co atoms in the active site transiently increases to 4+ or even 5+ and recovers its original value at the end of the OER cycle [28, 31, 32]. Numerous investigations were dedicated to experimentally evidence these Co species. Since they are only present under OER conditions and at the oxide surface, these studies have to be performed in operando conditions using surface sensitive techniques. Among these techniques, operando near ambient pressure X ray photoelectron spectroscopy (NAP-XPS) is the most surface sensitive since the measured photoelectrons originate from 1-2 nm below the surface [33-36]. Early NAP-XPS studies disagree on the Co oxidation state at the surface, some finding evidence for Co^{4+} [25] and some others do not [37]. The main limitation of these experiments is the very short inelastic mean free path of the photoelectrons outside the sample imposing either a nm thick electrolyte layer (dip and pull approach) or specific sample configuration allowing for photo-electrons detection from its back side. In all cases, the measurement is challenging and the reaction in the probed region is confined in a very small electrolyte volume.

Operando X-ray absorption spectroscopy (XAS) allows measurements very close to standard electrochemical conditions if the X ray energy is high enough as it is the case for the K edge of transition metals. It has been frequently used to determine the Co oxidation state and the local atomic environment of Co in oxide samples under OER conditions. Measurements primarily showed

that the average Co oxidation state increases with increasing potential for CoO and Co_3O_4 [15, 16, 19, 20, 22], CoOOH bulk and nanosheets [16, 17, 23, 27]. They also provided insights into the modification of the Co coordination shell under OER conditions [15, 16, 19]. All these studies report an increase of the Co average oxidation state during OER, but they fail to agree on its actual value. In some studies, the authors observed the formation of Co^{3+} and CoOOH –like layers on the surface and did not find any evidence of Co^{4+} [38]. In other studies, the authors claim that Co^{4+} is also formed under OER conditions [15]. Note that the Co oxide catalyst named CoCat is left out of the literature survey, because it is a very particular Co compound: it is formed of small entities of Co oxyhydroxide with a large defect density, is amorphous and contains a large concentration of phosphates [13, 17, 39-41].

In contrast to NAP-XPS, the operando XAS signal averages the Co oxidation state over the surface and the bulk of the oxide sample, the surface contribution being at most a few percent of the total XAS signal. Disentangling the bulk and surface contributions requires a precise estimation of the amount of Co atoms involved in the OER, which can be approximated by the number of Co atoms exposed to the electrolyte, i.e., the electrochemical surface area. Several methods have been proposed to estimate this parameter from double layer capacitance, Brunauer–Emmett–Teller (BET), or microscopy measurements but none of them is entirely satisfying [42]. The uncertainty of these measurements may thus be to a large part responsible for the wide range of Co oxidation state shifts with potential reported in the literature [17, 43].

In addition, the change in Co oxidation state may not be limited to the Co surface atoms, but extend deeper into the catalyst in form of a restructured layer of typically (sub)nanometer thickness, in which the structure differs from that within the catalyst bulk [44]. For the specific case of Co_3O_4 powders and epitaxial films, it was shown that an amorphous layer of nanometer thickness forms on the surface and constitutes the OER active phase [15, 16, 18, 37, 38, 45]. This layer is not permanently present on the surface but forms only above 1.15 V vs. the reversible hydrogen

electrode (RHE) and reversibly recrystallizes into the Co_3O_4 spinel lattice upon changing the potential negative of this value. Following the notation of our previous work [18, 45], we call this layer in the following the "skin layer", to distinguish it from the more common case of irreversibly formed surface phases, resulting from "catalyst activation". The latter phenomenon was reported too for Co oxide OER catalysts in studies of powder samples [21].

The use of epitaxial thin films with well-defined morphology and low surface roughness presents a unique advantage because the electrochemical surface area may be unambiguously measured, for instance using atomic force microscopy (AFM). Investigations of OER on Co oxide thin films with well-defined surface orientation remains scarce, however. The electrochemical behaviour of epitaxial Co_3O_4(111) films on Ir(100) or Au(111) prepared by deposition in vacuum was studied [46-48], but these works did not investigate the oxide structure and Co oxidation state under electrochemical conditions. Our group showed by AFM and *operando* surface X-ray diffraction (SXRD) that well-defined, thin epitaxial Co_3O_4(111) and CoOOH(001) films can be prepared by electrodeposition on Au(111) and that a reversible skin layer forms in the pre-OER range on the Co_3O_4(111) but not on the CoOOH(001) films [18, 49]. Moreover, we demonstrated that the skin layer is a 3D OER active zone[45]. The Co oxidation state in the skin layer was not clarified, however. It should be noted that epitaxial films as model catalysts for OER have been also used in the case of perovskites [50-53].

In this work, we present *operando* studies of Co oxides in alkaline electrolyte by combined X-ray absorption spectroscopy and surface X-ray diffraction. These data are obtained in the same experiment, which allows to rigorously correlate the surface structure, Co oxidation state, and electrochemical behaviour. The studies are performed on continuous epitaxial Co_3O_4(111) and CoOOH(001) films electrodeposited on Au(111). The use of such model systems allows unambiguous quantitative interpretation of the XAS results, specifically a clear separation of surface and bulk oxide

contributions. This provides valuable new insights into the oxidation state changes of the OER active zone.

2. Experimental

2.1 Au(111) substrate preparation and chemicals

The substrates were hat-shaped Au(111) single crystals (MaTeck) with an orientation uncertainty of <0.1°. They were cleaned in a 1:2 mixture of 30 % H_2O_2 and 96 % H_2SO_4 (both *Carlo Erba*, RSE) and then flame-annealed using a butane torch. Co nitrate (*Merck*, > 99.0 %), L-tartrate (*Sigma-Aldrich*, ACS reagent, > 99.5 %), NaOH (*Merck*, ACS reagent, Fe content < 0.0005 %), and Milli-Q water were used to prepare solutions. Pellets made of Co_3O_4 and CoO commercial powders (5% Cobalt powder 95% cellulose in weight, *Sigma-Aldrich*, 99.5 %) were used as reference samples for XANES.

2.2 Electrodeposition of epitaxial cobalt oxide films on Au(111)

Epitaxial cobalt oxide thin films were electrodeposited on Au(111) from a solution containing 1 mM $Co(NO_3)_2$ and 1.2 mM L-tartrate acid in 1 M (for depositing Co_3O_4) or 5 M NaOH (for depositing CoOOH). The electrochemical cell used for deposition was a closed ball shape glass cell, connected on its top to a condenser. The solution was purged with Argon in order to remove oxygen for 30 minutes before the deposition and during deposition. A saturated mercury sulphate (MSE) electrode was used as reference electrode and a Pt wire as counter electrode. The electrodes are connected to a home built potentiostat. The deposition was conducted at reflux (103°C) under potentiostatic conditions at a potential of -0.55 V_{MSE} in 1 M NaOH or -0.50 V_{MSE} in 5 M NaOH. The deposition current is positive and the deposition was stopped by putting the potentiostat at open circuit potential when an electrochemical charge of 8 mC/cm^2 was passed. Immediately afterwards, the sample was removed from the cell, quickly rinsed with Milli-Q water, blown dried with nitrogen gas, and stored in air.

2.3 Laboratory sample characterizations

The structure of as prepared deposits was characterized by XRD in θ-2θ geometry using a Rigaku Smartlab X-ray diffractometer with a rotating anode Cu Kα radiation source (λ= 0.154 nm). X-ray diffraction patterns were obtained using a parallel beam configuration, a Ge(220) double bounce monochromator on the incident beam side and a Hypix-3000 detector used in 1D mode.

The morphology of the deposits was investigated using a PicoSPM (Agilent) AFM operating in the AC Mode. Sharp silicon tips (µmasch, nominal tip radius ≈ 8 nm, cone angle 40°, spring constant ≈ 45 N m^{-1}, resonance frequency ≈ 190 kHz) were used for high-resolution imaging.

2.4 *Operando* XAS and XRD experiments

Operando XAS and SXRD studies were performed at the SOLEIL DiffAbs beamline using a photon energy between 7.6 and 8 keV, and a beam size of 250x300 μm^2. The experimental cell was placed on a 6 circles diffractometer in kappa geometry. The sample surface was horizontal and aligned parallel to the incident X ray beam prior to the measurements. A fixed incidence angle of 4° was used for XRD and XAS measurements, maximizing the footprint of the beam on the sample. At this incidence angle and within the energy range given above, the X ray absorption length is 10 times larger than the oxide film thickness. We thus consider that XRD and XAS probe the entire oxide films. XAS measurements were performed in fluorescence mode using a 4-element SDD fluorescence detector, which was placed just above the sample surface at 90° with respect to the incident X ray beam. For the SXRD measurements, a 2D detector (XPAD S140) was used to capture the diffraction peaks.

The *operando* measurements were performed in a custom electrochemical cell (see **Fig S1**) where the Co oxide covered surface of the Au(111) crystal is exposed to the electrolyte. An X-ray transparent polypropylene membrane covered the sample surface and remote-controlled pumps allowed to control the electrolyte thickness on top of the sample. The membrane may be inflated and deflated at will by injecting or removing electrolyte (more details are available in the supporting information, **section S1**). For all measurements, the electrolyte was a 0.1 M NaOH solution (pH 13)

kept under Argon atmosphere. Between measurements, the electrolyte in the cell and above the sample was regularly renewed by fresh electrolyte using the pump system. The potential was controlled with a potentiostat using a Ag/AgCl (3 M KCl) reference electrode and a Pt wire as counter electrode. All potentials are quoted against the reversible hydrogen electrode (RHE).

For the SXRD measurements, a beam energy of 7.83 keV was used. Structural changes were derived from the analysis of Co_3O_4(113) and CoOOH(105) Bragg peaks, because they have sufficiently high intensity and are accessible at the employed photon energy. As explained in **section S2** of the supporting information, the structural data are extracted from the fits of vertical and horizontal cross sections of the Bragg peak images acquired with the 2D detector. At each potential, the film strains ($\varepsilon_{//}$ and $\varepsilon_{\perp}$) are determined from the peak position and the in-plane and out-of-plane coherence lengths $d_{\perp}$and $d_{\|}$ from the vertical and horizontal FWHMs. The coherence lengths $d_{\perp}$and $d_{\|}$ provide the average height and width of the oxide film's crystallites, respectively. Other effects may also contribute to the FWHM as defects or inhomogeneous strain. In our approach, we attribute the FWHM exclusively to the crystallite size.

Operando XANES spectra were recorded at the Co K-edge between 7.64 and 7.82 keV. The typical acquisition time of a XANES spectrum is 30 minutes. Raw spectra were background corrected and normalized using the Athena software [54] . This correction is necessary for an accurate estimation of the absorption edge energy because the fluorescence spectrum is superimposed on a slowly decaying signal which is different below and above the edge. The Co K-edge energy E_{edge} was determined using the integral method [55]:

$$E_{edge} = \frac{1}{\mu_2 - \mu_1} \int_{\mu_1}^{\mu_2} E(\mu) d\mu \qquad (1)$$

Here μ is the X-ray absorption in the normalized XANES spectrum and μ_1 and μ_2 define the edge region boundaries. We used μ_1 =0.15 and μ_2 = 1 to avoid contributions from the pre-peak and absorption peak, respectively. In order to link E_{edge} and the cobalt oxidation state (hereafter called

α), a calibration curve has been established based on the commonly admitted linear relation between E_{edge} and α [56]. For this purpose, XANES spectra of reference samples with known Co oxidation state were recorded and their edge energy was determined using the above method (see **section S3**, **Fig S5a**). The inverse of the slope in **Fig S5b** gives $\Delta E_{edge} = 3.4\ eV$ per cobalt oxidation state unit. The average cobalt oxidation state α of the electrodeposited oxide thin films, resulting from the contributions of the Co ions with different oxidation states in the oxide film, was determined from the measured E_{edge} using this calibration.

Two acquisition methods were used to determine α as a function of potential of the oxide thin films. In the first one, the potential is stepped sequentially and a full XANES spectrum is acquired at each step. Since the acquisition time of a XANES spectrum is about 30 min and in order to have a reasonable acquisition time of a potential dependence dataset, only a few potentials were measured. The uncertainty on the absolute value of α in this case is ±0.03. It originates from the uncertainty on the determination of the absorption edge energy (±0.1 eV) which depends on two parameters: (i) the noise level of the measured fluorescence signal and (ii) the uncertainty on the background correction of the XANES spectra. The uncertainty on the X-ray beam energy is significantly smaller. In our measurements conditions of a full XANES spectrum, the second uncertainty is dominating the error bar. However, it should be noted that when a dataset as the one in Fig. S6 is analyzed, the same background correction is applied to all spectra. This implies that the relative error between the data points is practically less than ±0.03.

To improve time resolution, the oxidation state changes were also determined by a second method. Here, a XANES spectrum was acquired at one potential and then the incident X ray energy was set to E_{edge}. Subsequently, the fluorescence signal at this energy was measured during a potential sweep. This signal is then divided by the XANES spectrum slope at the initial value of E_{edge}, to obtain the E_{edge} shift, following the procedure in [57]. In this case, the integration time per point was 5 s. We used a typical potential sweep rate of 5 mV/s yielding a 25 mV potential resolution to

monitor the structural and oxidation state changes while sweeping the applied potential (see SI **section S4** and **Fig.S7**). With this method, the error bar originates only from the noise of the fluorescence signal which yields the fluctuations observed in Figs. S7b, S8b and S8d. This error bar is improved by averaging over several adjacent points and two potential sweeps, which has been done below. The uncertainty on the absolute value of the Co oxidation state (±0.03) comes from the XANES spectrum at 0.97 V and is the same for all data points. It does not add any fluctuations with potential.

3. Results

3.1 Characterization of as prepared oxide layers

As shown in **Fig. S11**, $\theta - 2\theta$ scans of as prepared films measured in air indicate that electrodeposition in 1 M NaOH yields Co_3O_4(111) and deposition in 5 M NaOH yields CoOOH(001). SXRD characterization conducted in air confirmed that the deposits are in epitaxy with Au(111) and essentially strain free (Section S6, supporting information). These findings are in agreement with our previous studies [18, 45, 49]. **Table 1** provides a list of all samples studied in this work together with their principal structural and spectroscopic parameters. $d_{\parallel}$ and $d_{\perp}$ are the in-plane and out-of-plane crystallite sizes determined from XRD data.

Figure 1 displays typical AFM images of the electrodeposited oxide films, along with horizontal cross-sections through the images along the dashed lines. The CoOOH film (**Fig. 1a**) consists of wide and rather shallow islands, with stepped facets. In the cross section shown in **Fig. 1c**, the steps are 0.4-0.5 nm high which is consistent with the distance between two atomic planes along the (001) direction of CoOOH (0.438 nm). The root mean square (RMS) roughness is 2.2 nm. The Co_3O_4 deposit (**Fig. 1b**) has a comparatively rougher morphology (5.2 nm RMS) with tightly packed triangular islands (30 nm to 70 nm wide). One notices that their edges are approximately parallel to six in plane directions separated by 60° and that they adopt two preferential orientations separated

by 180° (see drawn triangles in the zoom in the upper right corner inset). This is consistent with the hexagonal symmetry of the Co_3O_4(111) planes and two possible growth orientations on Au(111). The cross section in **Fig. 1d** shows that the average height between the island top and the deeper holes between the islands equals 20 nm approximately, very close to the value of $d_\perp$. All these observations are in agreement with our previous studies [49]. We note that the lateral island size measured by AFM is systematically larger than $d_\parallel$. This difference suggests that each island in the AFM image is composed of several tightly packed crystallites separated by grain boundary that cannot be resolved by the AFM tip. Based on these observations, we will in the following model the Co_3O_4 (111) islands as triangular prisms (see **scheme S1**) of height $d_\perp$ in order to estimate structural parameters as well as the electrochemical surface area. The morphology of Co oxide films is consistent with that previously reported [18].

Table 1: Main structural and spectroscopic parameters of as prepared samples in air and, given in parenthesis, in 0.1 M NaOH at 0.97 V, specifically the in-plane and out-of-plane crystallite sizes, $d_\parallel$ and $d_\perp$, the Co edge energy E_{edge}, and the Co oxidation state α. $d_\parallel$ and $d_\perp$ are determined with a precision of ± 0.2 nm, E_{edge} with a precision of ± 0.1 eV and α with a precision of ± 0.03.

Sample	$d_\perp$ (nm)	$d_\parallel$ (nm)	E_{edge} (eV)	α
Co_3O_4 - 1	22	21	7720.69 (7720.95)	2.54 (2.62)
Co_3O_4 - 2	29	21	7720.56 (7720.84)	2.5 (2.58)
CoOOH - 1	15	29	7722.36 (7722.37)	3.02 (3.03)
CoOOH - 2	17	35	7722.30 (7722.34)	3.0 (3.02)

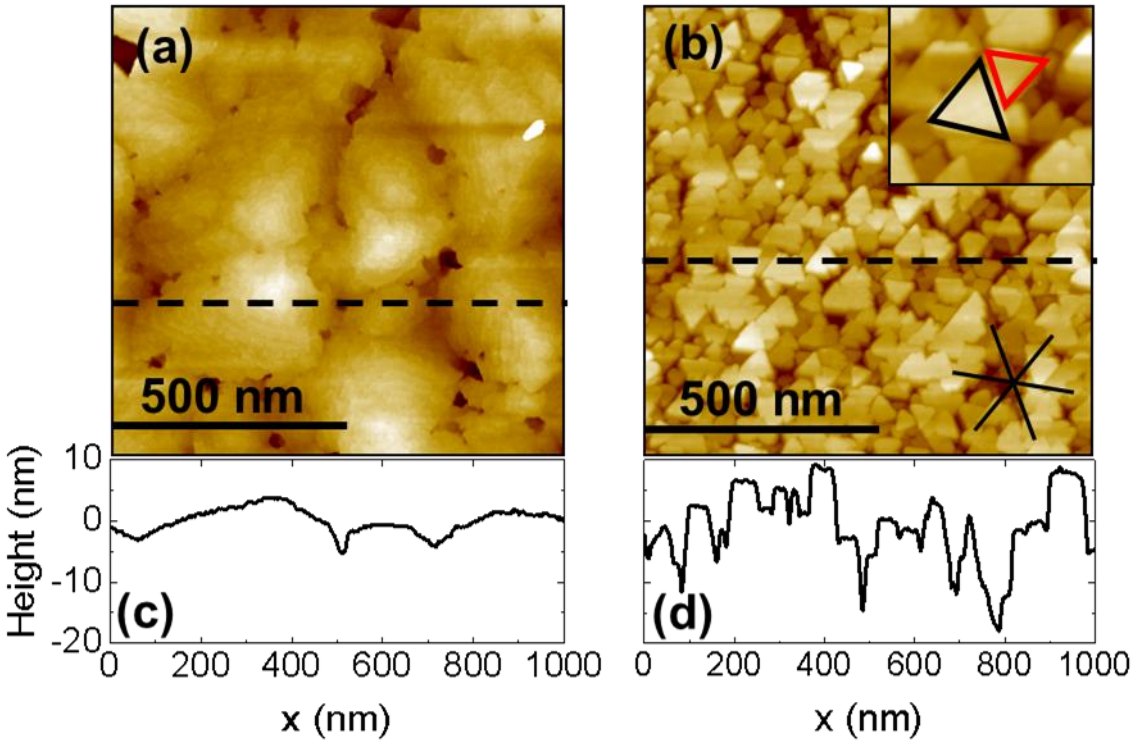

Figure 1: AFM images (1 µm x 1 µm) of (a) CoOOH(001) (sample CoOOH - 1) and (b) Co_3O_4(111) (sample Co_3O_4 - 1) films deposited on Au(111). Cross sections at the positions marked by dashed lines are shown below each image (plots (c) and (d)). The inset in (b) is a zoom by a factor of 2 of a region in the image. Red and black triangles in (b) indicate the two different orientations of Co_3O_4 islands. The 6 lines separated by 60° in (b) indicate the orientations of the triangular island edges.

3.2 Determination of Co average oxidation state from XANES measurements

Figure 2a displays normalized XANES spectra at the Co K-edge of as prepared Co_3O_4 and CoOOH deposits in air. The general shape of these spectra is consistent with that reported for the respective oxides in the literature [15, 20, 22, 24]. One main difference between the two spectra is a higher Co edge energy of CoOOH (blue curve) as compared to Co_3O_4 (red curve). One also notes differences in the amplitude of oscillations for energies larger than 7.74 keV, which can be attributed to the different average coordination shells around the Co atoms within the two oxides. Using the method detailed in **section 2.4,** the edge energies are found to be 7720.69 ± 0.1 eV (Co_3O_4 -1) and 7722.36 ± 0.1 eV (CoOOH -1). These values are converted into an average cobalt oxidation state α using the method described in **section S3** of the supporting information.

Table 1 gives the characteristic parameters (E_{edge} and α) of the different deposits in air and after polarization of the samples at a potential of 0.97 V in 0.1 M NaOH solution. According to our

previous studies, the structural parameters $d_{\parallel}$ and $d_{\perp}$ are the same as in air at this potential [18]. For CoOOH samples, α is very close to 3 in air and remains quasi-unchanged after immersion into the electrolyte. This is in perfect agreement with the nominal Co oxidation state in CoOOH and excludes the presence of O vacancies. These findings differ from other studies where an average oxidation state significantly lower than 3 was found on as-prepared samples [23, 58]. In the case of Co_3O_4, α = 2.54 in air, which departs from the expected 2.66 value. After immersion in the electrolyte, α = 2.62. A similar behavior was observed in studies on polycrystalline Co_3O_4 deposits [15]. This indicates that Co^{2+} relative concentration is above the nominal value of 33% in the as-prepared film, and approximately half of these cations are oxidized upon immersion of the sample in the electrolyte at the rest potential. The deviation of α may be accounted for by the presence of a 4 to 7 nm thick $Co(OH)_2$ phase in the as prepared samples. This is very unlikely, since no diffraction peak related to $Co(OH)_2$ was detected. Moreover, if present, $Co(OH)_2$ should transform into a more oxidized phase (as Co_3O_4) upon immersion into the electrolyte at the rest potential and would modify the diffracted signal. However, no change in the diffracted intensity of the Co_3O_4 peaks was observed [18]. A more plausible explanation is the presence of oxygen vacancies in the Co_3O_4 oxide bulk inducing a 2-6% larger proportion of Co^{2+} with respect to Co^{3+} cations in the film. These oxygen vacancies are partially filled upon sample immersion into the electrolyte. The latter phenomenon is often observed when specific procedures are used to induce O-vacancies during material synthesis [20].

Figure 2b illustrates the influence of the applied potential on the normalized XANES spectra at the Co K-edge of the Co_3O_4(111) film in 0.1M NaOH. We observe a small and progressive positive shift of E_{edge} with increasing potential, which is clearly visible in the figure inset. The amplitude of this shift is ~0.2 eV between 0.96 V and 1.36 V, which is similar to that measured with nanocrystalline Co_3O_4 [15].

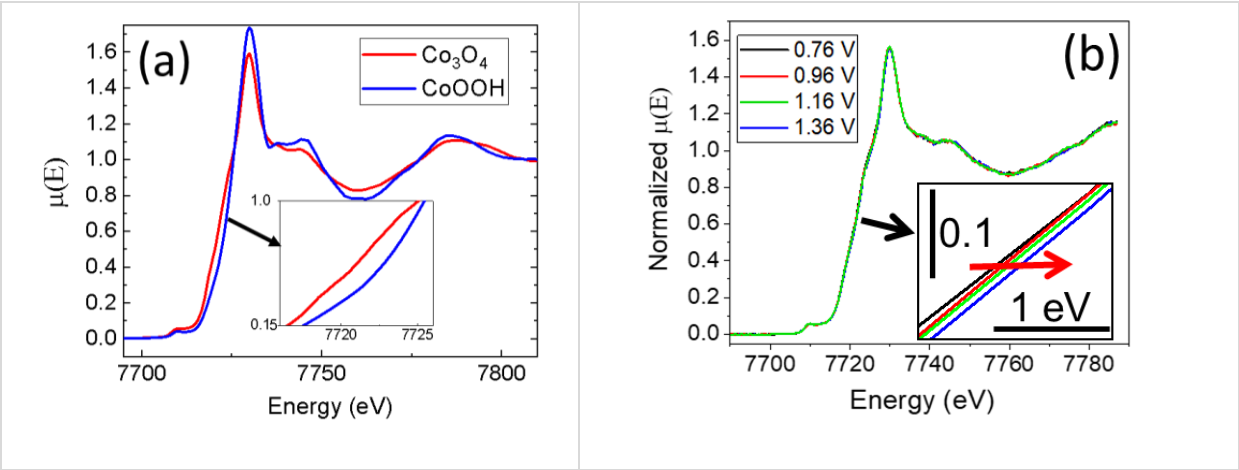

Figure 2: (a) Normalized XANES spectra recorded in air of typical CoOOH (blue curve) and Co_3O_4 (red curve) deposits on Au(111). The inset shows the edge region on an expanded energy scale. (b) Normalized XANES spectra of Co_3O_4 immersed in 0.1 M NaOH at different potentials. The inset shows a zoom in the edge region and the red arrow indicates the edge shift as a function of potential.

3.3 Correlations between cobalt oxidation state and deposit structure as a function of potential

Figure 3 presents the cyclic voltammograms (CVs) in 0.1 M NaOH of the two types of oxides together with the analysis of XAS and SXRD data, with the left and right columns corresponding to Co_3O_4 and CoOOH, respectively. The reference state is that measured at 0.97 V_{RHE}. The CV and the structural and oxidation state changes were monitored during two successive potential sweeps (5 mV/s) between 0.97 V and an upper potential limit 1.65 V, chosen to avoid the onset of bubble formation and significant ohmic drops in the thin electrolyte layer geometry. The filled and open symbols are the data points of the first and second potential cycle, respectively, and show a perfect reproducibility and reversibility of the data. The thick lines are averages of the data points over the two potential cycles.

The CVs (**Fig. 3a** red curve, and **Fig. 3b** blue curve) were first recorded without the polymer membrane with a thick electrolyte layer on top of the sample to minimize the ohmic drop and to allow relatively large OER currents. The black curves are CVs recorded subsequently with the polymer membrane mounted and deflated, to minimize X-ray electrolyte absorption. They differ from those obtained with a thick electrolyte layer in the OER regime only, where the restricted mass transport leads to a larger ohmic drop. In the pre-OER regime, the CVs of Co_3O_4 exhibit a pair of positive and

negative waves at 1.52 V which is consistent with our previous measurements [18] and the literature [46, 59-61]. The charge under the positive peak after linear baseline correction is approximatively 76 μC/cm^2. The uncertainty on this value is however large due to (i) the large background current, and (ii) the possible wetting of the sample edges and the associated large uncertainty on the exposed sample area. In the CV of CoOOH, only one rather weak redox wave around 1.15 V is visible. The catalytic activity is similar for both types of oxides after accounting for the electrochemical surface area of the deposits (see **sections S7** and **S8**). The Tafel slopes are 61 and 58 mV/decade for Co_3O_4 and CoOOH, respectively, and for both samples an overpotential of ca. 0.44 V is necessary for an OER current of 0.2 mA/cm^2 (see **section S8**). All these findings are in agreement with past reports [18, 45].

The XAS/XRD operando data were acquired with the membrane deflated during the CVs shown in black. The changes of oxidation state with potential, $\alpha(U)$, are presented in **Fig. 3c,d.** As explained in the supporting information (**section S4** and **Fig.S7**), the Co fluorescence signal was measured at a fixed X-ray energy close to E_{edge} during a potential sweep at 5 mV/s, following the procedure in [57]. For both types of oxides $\alpha(U)$ increases with increasing potential. The relative α change with respect to the value at 0.97 V ($\frac{\alpha(U)-\alpha(0.97\,V)}{\alpha(0.97\,V)}$) is significantly lower for CoOOH (0.3%) than for Co_3O_4 (1.5%). The variations are perfectly linear for CoOOH even down to 0.6 V (**Fig. S10**) suggesting that the same process is governing these changes over this large potential range. For Co_3O_4, $\alpha(U)$ increases approximately linearly between 1.1 and 1.6 V.

The other panels show the structural changes in grain size, $\Delta d_\perp$ (**Figs. 3e,f**) and $\Delta d_\parallel$ (**Figs. 3g,h**), and the relative change of the lattice unit cell volume $\frac{\Delta V_{bulk}}{V_{bulk}} = \frac{(V_{bulk}(U)-V_{bulk}(0.97\,V))}{V_{bulk}(0.97\,V)}$ (**Fig. 3i,j**). As explained in the experimental section, these parameters are determined from the position (strain) and the width (crystallite size) of the Bragg peak as a function of potential. The lattice strain variations as a function of potential $\Delta\varepsilon_\perp$ and $\Delta\varepsilon_\parallel$ are given in **Fig. S3** and the expression of $\Delta V_{bulk}/V_{bulk}$ in section **S2** of the supporting information. In agreement with our previous studies [18, 45], $\Delta d_\perp$ and $\Delta d_\parallel$ continuously decrease with potential for Co_3O_4(111) above 1.1 V, indicating

that the size of the crystalline oxide grains decreases. As discussed in the previous work, this decrease in grain size indicates the transformation of a sub-nm thick Co_3O_4 layer at the grain surface into an amorphous skin layer [18]. The reversible changes of $\Delta d_\perp$ and $\Delta d_\parallel$ with potential demonstrate that this skin layer fully recrystallizes into Co_3O_4 upon sweeping the potential negatively. Since the open circuit potential is close to 0.97 V, this skin layer is not expected to be present *ex situ*. Partial dissolution/precipitation of the oxide can be ruled out as the origin of the change in $\Delta d_\perp$ and $\Delta d_\parallel$, because this would lead to irreversible material loss into the electrolyte and thus be in opposition to the reversibility of the observed changes. The bulk oxide unit cell is contracting during the potential positive sweep, most probably because the phase change in the skin layer induces epitaxial strain [45]. These structural changes are perfectly reversible as long as the potential is > 1.0 V. The total contraction of the crystallites due to this strain is < 0.03 nm in horizontal and vertical direction, i.e., more than one order of magnitude smaller than the observed decrease of $\Delta d_\perp$ and $\Delta d_\parallel$ in **Figs. 3e,g,** and thus can be neglected in the estimation of the skin layer thickness.

By comparison, the CoOOH(001) layer remains structurally unchanged above 1 V and this stability region extents even down to 0.6 V (see also **section S5**). Below 0.6 V, some irreversible structural changes occur on the time scale of the potential sweep [18]. This transformation is accompanied by a steeper decrease of α which we attribute to the partial reduction of the CoOOH film into $Co(OH)_2$.

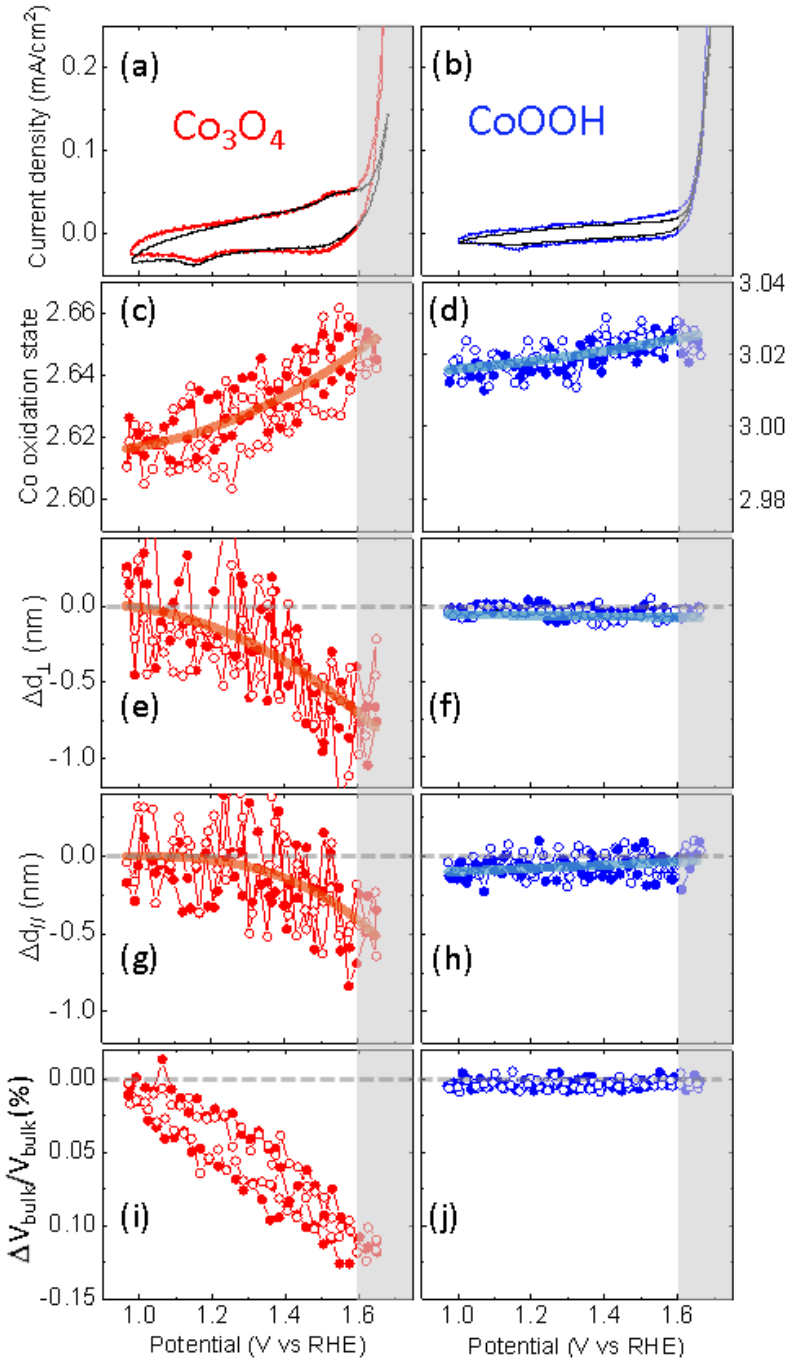

Figure 3: Correlation between electrochemistry in 0.1 M NaOH with the oxidation state and structure changes of Co_3O_4 and CoOOH deposits (obtained on samples Co_3O_4-1 and CoOOH-2) during potential cycles at 5 mV/s. (a,b) The black CVs are obtained with the deflated polymer window during the XAS-XRD measurements. For comparison, red and blue CVs are obtained in the XRD cell without the polymer window and with a thick electrolyte layer on top of the sample. The grey shaded region highlights the OER regime. (c,d) oxidation state as a function of potential, measured by XAS. (e-h) relative change of the coherence lengths $\Delta d_{\perp}$ and $\Delta d_{\parallel}$ and (i,j) relative change of the unit cell volume ΔV_{bulk} relative to the sample state at 0.97 V. (c-j) The good agreement between the two subsequent recorded potential cycles (indicated by filled and open symbols) demonstrate the high reversibility and reproducibility of the potential dependence.

4. Discussion

4.1 Oxidation of Co_3O_4 (111): a skin layer effect

In order to determine the origin of the change in α, we examine the relationship between $\alpha(U)$ and the skin layer formation. In **Fig. 4a**, we plot $\Delta\alpha(U) = \alpha(U) - \alpha(0.97\ V)$ and the average skin layer thickness $d_{skin}(U)$ as a function of potential. d_{skin} is determined from $d_{\perp,\parallel}(0.97\ V)$ and $\Delta d_{\perp,\parallel}(U)$ as the ratio of the volume of the skin layer and the geometric film surface (see supplementary information, **section S9**) and represents a convenient way to quantify the fraction of Co atoms that are reversibly transformed at a given potential. Closed and open symbols in **Fig. 4a** correspond to positive (filled symbols) and negative (open symbols) potential sweeps, respectively, averaged over two consecutive sweeps. We find in both positive and negative potential sweeps that the average skin layer thickness and the oxidation state follow the same potential dependence. In particular, the hysteresis in $d_{skin}(U)$ is also present in $\Delta\alpha(U)$. This one-to-one correlation of $\Delta\alpha(U)$ and $d_{skin}(U)$ in the entire potential range indicates that the increase in $\alpha(U)$ results from the increase of the oxidation state of Co cations in the skin layer, and that the oxidation state of the underlying crystalline Co_3O_4 bulk remains unchanged.

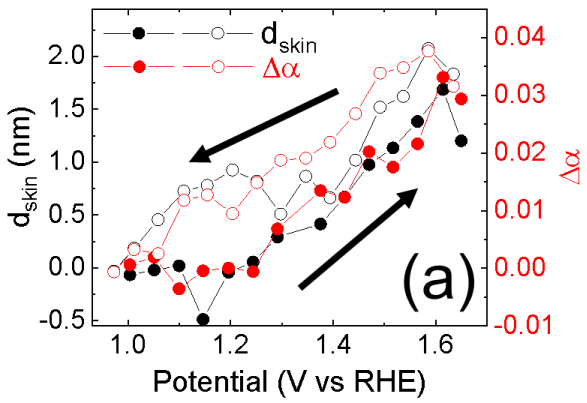

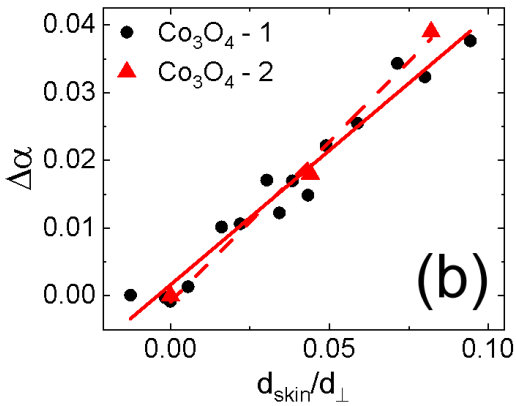

Figure 4: (a) experimental change of $d_{skin}(U)$ (left y axis and black symbols) and the relative oxidation state $\Delta\alpha(U)$ (right y axis and red symbols) as a function of potential between 0.97 und 1.67 V_{RHE}. (b) $\Delta\alpha(U)$ as a function of the ratio $d_{skin}(U)/d_{\perp}$. The red lines are linear fits of the data for Co_3O_4 – 1 (solid line) and for Co_3O_4 – 2 (dashed line).

To determine the average oxidation state of Co cations in the skin layer (α_{skin}) as a function of potential, we write $\alpha(U)$ as the sum of two contributions: α_{skin} and α_{bulk} the oxidation state of Co atoms in the Co_3O_4 spinel bulk lattice. These two contributions are weighted by their respective volume fractions, which are given by $d_{skin}/d_\perp$ and $(d_\perp - d_{skin})/d_\perp$. The average oxidation state $\alpha(U)$ can thus be written as follows:

$$\alpha(U) = \alpha_{skin}(U)\frac{d_{skin}(U)}{d_\perp} + \alpha_{bulk}(U)\frac{d_\perp - d_{skin}(U)}{d_\perp} \quad (2a)$$

The change $\Delta\alpha(U)$ is then:

$$\Delta\alpha(U) = \alpha(U) - \alpha(0.97\,V)$$

$$= \frac{d_{skin}(U)}{d_\perp}\,[\alpha_{skin}(U) - \alpha_{bulk}(U)] + [\alpha_{bulk}(U) - \alpha_{bulk}(0.97\,V)] \quad (2b)$$

Here, $\alpha(0.97\,V)$ equals the value of α_{bulk} at this potential, because $d_{skin}(0.97\,V) = 0$. In **Eq. 2**, we considered that both α_{skin} and α_{bulk} may depend on the potential. **Figure 4b** shows the variations of $\Delta\alpha(U)$ as a function of $d_{skin}(U)/d_\perp$ for the two Co_3O_4 samples. The data of Co_3O_4-1 (black symbols) are derived from **Fig. 3c**. The data of sample Co_3O_4-2 (red symbols) were determined from full XANES spectra, acquired at fixed potentials (**Fig. 2b**). The same dependence is obtained by the two methods. To reduce the experimental noise of the Co_3O_4-1 data set, $\Delta\alpha(U)$ and $d_{skin}(U)/d_\perp$ values were averaged over the two potential cycles. Our analysis shows that $\Delta\alpha(U)$ is directly proportional to $d_{skin}(U)/d_\perp$, i.e., the linear fits have a near zero intercept. The latter demonstrates that $\alpha_{bulk}(U)$ is independent of potential and consequently equal to $\alpha_{bulk}(0.97\,V)$. Moreover, the linear relationship between $\Delta\alpha(U)$ and $d_{skin}(U)/d_\perp$ indicates that $\alpha_{\mathrm{skin}}(\mathrm{U}) - \alpha_{\mathrm{bulk}}$ is constant and α_{skin} thus is also independent of the potential. This provides strong evidence that the variations in the average Co oxidation state α originate from the change of the oxidation state of Co cations in the skin layer. In addition, it implies that the skin layer has a fixed average oxidation state, and that the observed variations of α are exclusively due to the change of the skin layer thickness. For Co_3O_4-1, the slope of the linear fit in **Fig. 4b** equals $\alpha_{skin} - \alpha_{bulk} = 0.4$ corresponding to $\alpha_{skin} = 3.02$. The analysis for

Co_3O_4-2 yields a very similar value for α_{skin} of 3.05 (**Table 2**), even though the two samples have different grain size and d_{skin} values (see **Table 2** and **section S9**).

Table 2: Selected parameters of the Co_3O_4 samples. α_{bulk} is the mean Co oxidation state of the oxide at U = 0.97 V, the third column is the slope of the plot $\Delta\alpha(U)$ as a function of $d_{skin}(U)/d_{\perp}$. α_{skin} is the oxidation state of the skin layer, d_{skin} is the skin layer thickness at the most positive potential (1.67 V/RHE for Co_3O_4 - 1 and 1.37 V/RHE for Co_3O_4 - 2). $\Delta\alpha_{surf}$ is oxidation state increase of the skin layer with respect to the bulk value.

sample	α_{bulk}	Slope	α_{skin}	d_{skin} (nm)	$\Delta\alpha_{surf}$
Co_3O_4 - 1	2.62 ± 0.03	0.4	3.02 ± 0.03	1.85	0.4
Co_3O_4 - 2	2.58 ± 0.03	0.47	3.05 ± 0.03	2.33	0.47

The value of α_{skin} is slightly larger than 3 but the difference falls almost within the error bar and is similar to the measured CoOOH oxidation state at the most negative potentials (see section 4.2). Therefore, we consider that the actual value of α_{skin} is 3. This value of α_{skin} may be the result of a skin layer formed of Co^{3+} exclusively, or composed of a mixture of Co^{3+} and an equal proportion of Co^{2+}, and Co^{4+}. However, several observations speak against the latter scenario. First, the stabilization of these three oxidation states in quasi-equilibrium conditions is highly improbable over such a large potential range of 0.7 V. Second, the onset potential of the skin layer formation is ~1.2 V. This potential is close to the standard potential of the reaction $Co_3O_4 + OH^- + H_2O \rightarrow 3CoOOH + e^-$, which is 1.1 V but is significantly more negative than the standard potentials to form Co^{4+} (1.4-1.5 V) [59]. The difference between 1.1 V and the experimental value of 1.2 V is probably due to the fact that we are considering surface redox reaction whereas standard potentials are given for bulk one. Third, α_{skin} is independent of the potential, starting from 1.2 V on, and equals 3 (within the measurement uncertainty) which is consistent with the $Co_3O_4/CoOOH$ reaction above and a skin layer exclusively formed of Co^{3+}. The formation of Co^{4+} above 1.5 V should lead to a slope break that is not observed within the precision of the measurements. Consequently, all our observations suggest that the skin layer is formed exclusively of Co^{3+} by the oxidation of Co^{2+} present at the oxide surface. The latter occupy tetrahedral sites, in which Co^{3+} is unstable. The oxidation state change

requires thus some reorganization of the Co atoms of the Co sublattice which is consistent with the low crystallinity of the skin layer. This disordered surface region, which is the OER active phase on Co_3O_4, contains only Co^{3+}. The surface concentration of Co^{4+} remains below the measurement error bar, 3% in our case.

As mentioned in the introduction, all previous studies agree that the average oxidation state of Co atoms inside this skin layer is larger than in the pristine material but they failed to agree on its actual value. In addition, in most of them, the average Co oxidation state was found to increase gradually over several 100 mV and quasi-saturates before a significant OER current is measured [15, 23, 62]. This clearly indicate that the observed oxidation state changes are not due to OER but to the transformation of the Co oxide prior to OER onset potential. In some studies, the authors concluded that the Co oxidation state increases to 3 [37, 38], whereas in some other studies, they suggested that Co^{4+} is also formed [15]. However, the evidence for the actual Co oxidation state was indirect and limited by the uncertainty of determining the proportion of Co atoms within the skin layer. This is necessary to give a precise estimation of the average oxidation state in the skin layer. It requires the measurement of the skin layer thickness at different Co_3O_4 crystallites facets which is difficult in the case of powders or polycrystalline films. Our work demonstrates the benefit of using epitaxial films in which the Co_3O_4 crystallites are densely packed forming a single layer, have the same out-plane orientation and the crystallite facets are well characterized. Consequently, the skin volume can be determined with a large precision at each potential. The absence of Co^{4+} in our case as compared to other studies may be related to the epitaxy of the Co_3O_4 crystallites, which expose to the electrolyte limited and well-defined facets. Whether Co^{4+} forms on Co_3O_4 powders that expose other facets cannot be excluded rigorously.

4.2 Oxidation of CoOOH(001): a surface effect

The Co oxidation state of CoOOH films at 0.97 V is very close to the expected value of 3 but slightly larger. At this negative potential where OER cannot take place, Co^{4+} species are not

thermodynamically stable even in a transient state. We thus consider that α = 3 and that the difference is due to the uncertainty for determining α from the XAS spectrum. The small α variations with potential are linear, reversible and reproducible. Since no skin layer formation was observed in this case, an oxidation state which departs from 3 can only be due to a different oxidation state of the Co top surface atoms (α_{surf}). Similarly to the case of Co_3O_4, we can decompose $\alpha(U)$ into the weighted sum of a bulk and a surface contribution:

$$\alpha(U) = \frac{n-1}{n} \times \alpha_{bulk} + \frac{1}{n} \times \alpha_{surf}(U) \qquad (3a)$$

where $n = \frac{d_{\perp}(nm)}{0.438}$ is the number of Co planes parallel to the surface within the film (see **Fig. S13a** for more details) and α_{bulk}=3, the change with potential $\frac{d\alpha_{surf}(U)}{dU}$ is:

$$\frac{d\alpha_{surf}(U)}{dU} = n \frac{d\alpha(U)}{dU} \qquad (3b)$$

Equation (3b) yields $\frac{d\alpha_{surf}(U)}{dU}$ with a very good accuracy since the determination of $\frac{d\alpha(U)}{dU}$ from the linear fit and that of n from the width of the diffraction peak are very precise. Using the experimental parameters of $\frac{d\alpha}{dU}$ and n in **Table 3** for the two CoOOH deposits, we can estimate $\frac{d\alpha_{surf}(U)}{dU}$ and find that α_{surf} increases by ~0.3 in the explored potential range.

Table 3: Selected parameters of CoOOH samples. n is the number of layers in the CoOOH deposit, $d\alpha/dU$ and $d\alpha_{surf}/dU$ are the measured total changes in cobalt oxidation state and the derived changes in oxidation state of Co surface atoms the with potential, respectively, and $d\theta_H/dU$ is the calculated variations of the surface coverage of OH groups. $\Delta\alpha_{surf}$ is the oxidation state change between 0.97 V/RHE and 1.67 V/RHE of the CoOOH topmost atomic layer.

Sample	n	$d\alpha/dU$ (V^{-1})	$d\alpha_{surf}/dU$ (V^{-1})	$d\theta_H/dU$ (V^{-1})	$\Delta\alpha_{surf}$
CoOOH – 1	34.2	0.011	0.38	– 0.38	0.27
CoOOH – 2	38.8	0.012	0.47	– 0.47	0.33

In view of the potential invariant CoOOH structure, a change in surface oxidation state can only take place by hydroxylation/dehydroxylation of the oxide surface. In fact, as explained in the supplementary information (**section S10**), α_{surf} is related to the OH surface coverage (θ_{OH}). For example, α_{surf} = 3 corresponds to a surface where only half of the O atoms are hydrogenated, i.e., θ_{OH} = 0.5. This is due to the fact that in CoOOH a surface H atom is bonded to only one O atom whereas in bulk, it is bonded to two O. For other values of θ_{OH}, α_{surf} is linear and may be written as $\alpha_{surf} = 2.5 \times \theta_{OH} + 3.5 \times (1 - \theta_{OH})$.

As $\frac{d\theta_{OH}(U)}{dU} = -\frac{d\alpha_{surf}(U)}{dU}$, θ_{OH} decreases linearly by ~ 0.3 in the pre-OER potential range (**Table 3**), and its change with increasing potential is not related to the OER. This behaviour clearly indicates that it is related to the thermodynamics of the CoOOH surface rather than to an OER induced surface chemistry transformation. The OH coverage of the CoOOH(001) surface as a function of potential has already been addressed in literature using *ab initio* calculations. θ_{OH} = 0.5 for α_{surf} = 3 has been shown in DFT calculations combined with molecular dynamics (DFT-MD) which explicitly included the liquid water dynamics [63]. These calculations provided insight into the dynamics of H at the surface and demonstrated fast H hopping between neighbouring O atoms. Chen et al. performed DFT calculations for 3 different θ_{OH} values 0, 0.5 and 1.0 ML, and showed that the crossover from 1.0 to 0.5 ML occurred at 0.7 V and that from 0.5 to 0 ML at 1.6 V [30]. Bajdich et al. did similar calculations with intermediate θ_{OH} values but found that the transition potentials are significantly more positive. They showed that the crossover from 0.25 to 0.5 ML takes place at 0.5 V, from 0.5 to 0.75 ML at 1.3 V and 0.75 to 1 ML at 1.5 V [28]. In this latter study, θ_{OH} is not linear with potential and increases more steeply at potentials >1.3 V. This is at variance from our results where θ_{OH} varies linearly over a large potential range without any slope change. This difference may be due to the fact that the study by Bajdich et al. did not take solution water molecules and their dynamics and interaction with the O/OH groups at the CoOOH surface into account.

From the experimental point of view, potential dependent Co oxidation state has been reported in the case of amorphous CoOOH nano-sheets with a high electrochemical surface area [13, 23, 43, 58]. In these studies, α was found to increase steeply at around 1.4 V followed by a more gradual increase or saturation at more positive potentials. In most of the cases, α values larger than 3 were reached at the OER onset and can only be explained by the formation of Co^{4+}. The observed transitions from Co^{2+}/Co^{3+} to Co^{3+}/Co^{4+} were attributed to modifications in the CoOOH bulk through filling of oxygen vacancies and deprotonation. In our results on perfectly crystalline and epitaxial CoOOH films, the deprotonation is restricted to the CoOOH(001) surface and to a fraction of the surface OH groups.

Since the skin layer which builds up on the Co_3O_4 film is CoOOH-like, comparing both oxides may give some additional insight. In both type of samples, the change in oxidation state is related to the oxide's transformation in a near surface region. To compare the two materials, we therefore compare the average oxidation state changes ($\Delta\alpha_{surf}$) between 1 and 1.6 V of the Co cations in the transformed oxide surface region. In the case of Co_3O_4, $\Delta\alpha_{surf}$ = 0.4-0.47 (**Table 2**). In the case of CoOOH, $\Delta\alpha_{surf}$ = 0.27-0.33 (**Table 3**), values rather close to those obtained for Co_3O_4. The similarity of the values for both oxides suggests that the potential-dependent oxidation state change at the CoOOH surface is similar to that in the Co_3O_4 skin layer, i.e., corresponds to a Co^{2+} to Co^{3+} transformation, and that the CoOOH topmost layer is formed of Co^{3+} at the OER onset. Taking into account that these transformed regions are the OER-active phase, our data provides strong evidence that, in steady state conditions, the active surface species at the OER onset is Co^{3+} for both oxides, and that the surface concentration of Co^{4+} is negligible. Since Co^{4+} is expected to be an intermediate species in the OER mechanism on Co oxides, our findings suggest that it has a short life-time at the OER onset.

5. Conclusion

We performed combined SXRD/XAS in situ studies on epitaxial Co_3O_4 and CoOOH films deposited on Au(111) with well-defined morphology in the pre-OER and OER regime. From the Bragg peak FWHM which we attribute to the crystallite size, we give evidence of the transformation of the oxide surface and from the edge energy of the XAS spectra we determine the Co oxidation state. This allowed us to rigorously correlate these two parameters and determine (i) the oxide region which contributes to the increase of the Co oxidation state and (ii) the Co oxidation state at the surface of both oxides. In the case of Co_3O_4, our results show that the Co oxidation state increase takes place exclusively in the nm-thick skin layer that forms before the OER onset. This skin layer is disordered, CoOOH-like and is composed of Co^{3+} species at the OER onset, i.e., the amount of Co centres with a higher oxidation state is negligible, even at the OER onset. In the case of CoOOH, the Co oxidation state change with increasing potential is limited to the topmost surface and takes place through the gradual deprotonation of the surface not requiring any structural modifications. In both cases, we find no evidence for the presence of Co^{4+}. From the similar OER activity of Co_3O_4 and CoOOH layers we conclude that the active surface species is Co^{3+} and that the surface concentration of Co^{4+} remains below 1% in OER steady state conditions.

Supporting information

Scheme of XRD electrochemical cell, operando XRD characterizations of cobalt oxide thin films, oxidation state calibration, determination of the Co oxide state as a function of potential, electrochemical reduction of CoOOH, ex-situ characterizations of electrodeposited oxides, morphology and electrochemical surface area of the deposits, catalytic and electrochemical properties of electrodeposited oxides, determination of Co_3O_4 skin volume, oxide structure

Acknowledgements

We gratefully acknowledge financial support by the Agence Nationale de la Recherche (ANR) and by the Deutsche Forschungsgemeinschaft (DFG) via project EC-MEC (ANR-15-CE30-0024-01 and DFG 284207613) and by the German Federal Ministry of Education and Research (BMBF) via project 05K19FK3. We acknowledge Soleil Synchrotron for providing the experimental facilities and warmly thank the staff of the DiffAbs beamline for technical support.

References

[1] Tahir, M., Pan, L., Idrees, F., Zhang, X., Wang, L., Zou, J.-J., Wang, Z. L., Electrocatalytic oxygen evolution reaction for energy conversion and storage: A comprehensive review, *Nano Energy*, 2017, *37*, 136-157

[2] McCrory, C. C. L., Jung, S., Peters, J. C., Jaramillo, T. F., Benchmarking Heterogeneous Electrocatalysts for the Oxygen Evolution Reaction, *Journal of the American Chemical Society*, 2013, *135*, 16977-16987

[3] Burke, M. S., Zou, S., Enman, L. J., Kellon, J. E., Gabor, C. A., Pledger, E., Boettcher, S. W., Revised Oxygen Evolution Reaction Activity Trends for First-Row Transition-Metal (Oxy)hydroxides in Alkaline Media, *The Journal of Physical Chemistry Letters*, 2015, *6*, 3737-3742

[4] Deng, X., Tüysüz, H., Cobalt-Oxide-Based Materials as Water Oxidation Catalyst: Recent Progress and Challenges, *ACS Catalysis*, 2014, *4*, 3701-3714

[5] Artero, V., Chavarot-Kerlidou, M., Fontecave, M., Splitting Water with Cobalt, *Angewandte Chemie International Edition*, 2011, *50*, 7238-7266

[6] Song, F., Bai, L., Moysiadou, A., Lee, S., Hu, C., Liardet, L., Hu, X., Transition Metal Oxides as Electrocatalysts for the Oxygen Evolution Reaction in Alkaline Solutions: An Application-Inspired Renaissance, *Journal of the American Chemical Society*, 2018, *140*, 7748-7759

[7] Li, X., Wang, H.-Y., Yang, H., Cai, W., Liu, S., Liu, B., In Situ/Operando Characterization Techniques to Probe the Electrochemical Reactions for Energy Conversion, *Small Methods*, 2018, *2*, 1700395

[8] Gerken, J. B., McAlpin, J. G., Chen, J. Y. C., Rigsby, M. L., Casey, W. H., Britt, R. D., Stahl, S. S., Electrochemical Water Oxidation with Cobalt-Based Electrocatalysts from pH 0–14: The Thermodynamic Basis for Catalyst Structure, Stability, and Activity, *Journal of the American Chemical Society*, 2011, *133*, 14431-14442

[9] Surendranath, Y., Kanan, M. W., Nocera, D. G., Mechanistic Studies of the Oxygen Evolution Reaction by a Cobalt-Phosphate Catalyst at Neutral pH, *Journal of the American Chemical Society*, 2010, *132*, 16501-16509

[10] Zhang, M., de Respinis, M., Frei, H., Time-resolved observations of water oxidation intermediates on a cobalt oxide nanoparticle catalyst, *Nature Chemistry*, 2014, *6*, 362-367

[11] van Oversteeg, C. H. M., Doan, H. Q., de Groot, F. M. F., Cuk, T., In situ X-ray absorption spectroscopy of transition metal based water oxidation catalysts, *Chemical Society Reviews*, 2017, *46*, 102-125

[12] Chang, C.-J., Zhu, Y., Wang, J., Chen, H.-C., Tung, C.-W., Chu, Y.-C., Chen, H. M., In situ X-ray diffraction and X-ray absorption spectroscopy of electrocatalysts for energy conversion reactions, *Journal of Materials Chemistry A*, 2020, *8*, 19079-19112

[13] Risch, M., Ringleb, F., Kohlhoff, M., Bogdanoff, P., Chernev, P., Zaharieva, I., Dau, H., Water oxidation by amorphous cobalt-based oxides: in situ tracking of redox transitions and mode of catalysis, *Energy & Environmental Science*, 2015, *8*, 661-674
[14] Pasquini, C., D'Amario, L., Zaharieva, I., Dau, H., Operando Raman spectroscopy tracks oxidation-state changes in an amorphous Co oxide material for electrocatalysis of the oxygen evolution reaction, *The Journal of Chemical Physics*, 2020, *152*, 194202
[15] Bergmann, A., Martinez-Moreno, E., Teschner, D., Chernev, P., Gliech, M., de Araújo, J. F., Reier, T., Dau, H., Strasser, P., Reversible amorphization and the catalytically active state of crystalline Co3O4 during oxygen evolution, *Nature Communications*, 2015, *6*, 8625
[16] Bergmann, A., Jones, T. E., Martinez Moreno, E., Teschner, D., Chernev, P., Gliech, M., Reier, T., Dau, H., Strasser, P., Unified structural motifs of the catalytically active state of Co(oxyhydr)oxides during the electrochemical oxygen evolution reaction, *Nature Catalysis*, 2018, *1*, 711-719
[17] Friebel, D., Bajdich, M., Yeo, B. S., Louie, M. W., Miller, D. J., Sanchez Casalongue, H., Mbuga, F., Weng, T.-C., Nordlund, D., Sokaras, D., Alonso-Mori, R., Bell, A. T., Nilsson, A., On the chemical state of Co oxide electrocatalysts during alkaline water splitting, *Physical Chemistry Chemical Physics*, 2013, *15*, 17460-17467
[18] Reikowski, F., Maroun, F., Pacheco, I., Wiegmann, T., Allongue, P., Stettner, J., Magnussen, O. M., Operando Surface X-ray Diffraction Studies of Structurally Defined Co3O4 and CoOOH Thin Films during Oxygen Evolution, *ACS Catalysis*, 2019, *9*, 3811-3821
[19] Wang, H.-Y., Hung, S.-F., Chen, H.-Y., Chan, T.-S., Chen, H. M., Liu, B., In Operando Identification of Geometrical-Site-Dependent Water Oxidation Activity of Spinel Co3O4, *Journal of the American Chemical Society*, 2016, *138*, 36-39
[20] Xiao, Z., Huang, Y.-C., Dong, C.-L., Xie, C., Liu, Z., Du, S., Chen, W., Yan, D., Tao, L., Shu, Z., Zhang, G., Duan, H., Wang, Y., Zou, Y., Chen, R., Wang, S., Operando Identification of the Dynamic Behavior of Oxygen Vacancy-Rich Co3O4 for Oxygen Evolution Reaction, *Journal of the American Chemical Society*, 2020, *142*, 12087-12095
[21] Ortiz Peña, N., Ihiawakrim, D., Han, M., Lassalle-Kaiser, B., Carenco, S., Sanchez, C., Laberty-Robert, C., Portehault, D., Ersen, O., Morphological and Structural Evolution of Co3O4 Nanoparticles Revealed by in Situ Electrochemical Transmission Electron Microscopy during Electrocatalytic Water Oxidation, *ACS Nano*, 2019, *13*, 11372-11381
[22] Seo, B., Sa, Y. J., Woo, J., Kwon, K., Park, J., Shin, T. J., Jeong, H. Y., Joo, S. H., Size-Dependent Activity Trends Combined with in Situ X-ray Absorption Spectroscopy Reveal Insights into Cobalt Oxide/Carbon Nanotube-Catalyzed Bifunctional Oxygen Electrocatalysis, *ACS Catalysis*, 2016, *6*, 4347-4355
[23] Zhou, J., Wang, Y., Su, X., Gu, S., Liu, R., Huang, Y., Yan, S., Li, J., Zhang, S., Electrochemically accessing ultrathin Co (oxy)-hydroxide nanosheets and operando identifying their active phase for the oxygen evolution reaction, *Energy & Environmental Science*, 2019, *12*, 739-746
[24] Huang, J., Chen, J., Yao, T., He, J., Jiang, S., Sun, Z., Liu, Q., Cheng, W., Hu, F., Jiang, Y., Pan, Z., Wei, S., CoOOH Nanosheets with High Mass Activity for Water Oxidation, *Angewandte Chemie International Edition*, 2015, *54*, 8722-8727
[25] Favaro, M., Yang, J., Nappini, S., Magnano, E., Toma, F. M., Crumlin, E. J., Yano, J., Sharp, I. D., Understanding the Oxygen Evolution Reaction Mechanism on CoOx using Operando Ambient-Pressure X-ray Photoelectron Spectroscopy, *Journal of the American Chemical Society*, 2017, *139*, 8960-8970
[26] Yeo, B. S., Bell, A. T., Enhanced Activity of Gold-Supported Cobalt Oxide for the Electrochemical Evolution of Oxygen, *Journal of the American Chemical Society*, 2011, *133*, 5587-5593
[27] Moysiadou, A., Lee, S., Hsu, C.-S., Chen, H. M., Hu, X., Mechanism of Oxygen Evolution Catalyzed by Cobalt Oxyhydroxide: Cobalt Superoxide Species as a Key Intermediate and Dioxygen Release as a Rate-Determining Step, *Journal of the American Chemical Society*, 2020, *142*, 11901-11914
[28] Bajdich, M., García-Mota, M., Vojvodic, A., Nørskov, J. K., Bell, A. T., Theoretical Investigation of the Activity of Cobalt Oxides for the Electrochemical Oxidation of Water, *Journal of the American Chemical Society*, 2013, *135*, 13521-13530

[29] Mattioli, G., Risch, M., Amore Bonapasta, A., Dau, H., Guidoni, L., Protonation states in a cobalt-oxide catalyst for water oxidation: fine comparison of ab initio molecular dynamics and X-ray absorption spectroscopy results, *Physical Chemistry Chemical Physics*, 2011, *13*, 15437-15441
[30] Chen, J., Selloni, A., First Principles Study of Cobalt (Hydr)oxides under Electrochemical Conditions, *The Journal of Physical Chemistry C*, 2013, *117*, 20002-20006
[31] Pham, H. H., Cheng, M.-J., Frei, H., Wang, L.-W., Surface Proton Hopping and Fast-Kinetics Pathway of Water Oxidation on Co3O4 (001) Surface, *ACS Catalysis*, 2016, *6*, 5610-5617
[32] Plaisance, C. P., van Santen, R. A., Structure Sensitivity of the Oxygen Evolution Reaction Catalyzed by Cobalt(II,III) Oxide, *Journal of the American Chemical Society*, 2015, *137*, 14660-14672
[33] Saveleva, V. A., Savinova, E. R., Insights into electrocatalysis from ambient pressure photoelectron spectroscopy, *Current Opinion in Electrochemistry*, 2019, *17*, 79-89
[34] Falling, L. J., Mom, R. V., Sandoval Diaz, L. E., Nakhaie, S., Stotz, E., Ivanov, D., Hävecker, M., Lunkenbein, T., Knop-Gericke, A., Schlögl, R., Velasco-Vélez, J.-J., Graphene-Capped Liquid Thin Films for Electrochemical Operando X-ray Spectroscopy and Scanning Electron Microscopy, *ACS Applied Materials & Interfaces*, 2020, *12*, 37680-37692
[35] Streibel, V., Hävecker, M., Yi, Y., Velasco Vélez, J. J., Skorupska, K., Stotz, E., Knop-Gericke, A., Schlögl, R., Arrigo, R., In Situ Electrochemical Cells to Study the Oxygen Evolution Reaction by Near Ambient Pressure X-ray Photoelectron Spectroscopy, *Topics in Catalysis*, 2018, *61*, 2064-2084
[36] Lu, Y.-H., Morales, C., Zhao, X., van Spronsen, M. A., Baskin, A., Prendergast, D., Yang, P., Bechtel, H. A., Barnard, E. S., Ogletree, D. F., Altoe, V., Soriano, L., Schwartzberg, A. M., Salmeron, M., Ultrathin Free-Standing Oxide Membranes for Electron and Photon Spectroscopy Studies of Solid–Gas and Solid–Liquid Interfaces, *Nano Letters*, 2020, *20*, 6364-6371
[37] Zhang, X., Chen, Y.-S., Kamat, P. V., Ptasinska, S., Probing Interfacial Electrochemistry on a Co3O4 Water Oxidation Catalyst Using Lab-Based Ambient Pressure X-ray Photoelectron Spectroscopy, *The Journal of Physical Chemistry C*, 2018, *122*, 13894-13901
[38] Tung, C.-W., Hsu, Y.-Y., Shen, Y.-P., Zheng, Y., Chan, T.-S., Sheu, H.-S., Cheng, Y.-C., Chen, H. M., Reversible adapting layer produces robust single-crystal electrocatalyst for oxygen evolution, *Nature Communications*, 2015, *6*, 8106
[39] Kanan Matthew, W., Nocera Daniel, G., In Situ Formation of an Oxygen-Evolving Catalyst in Neutral Water Containing Phosphate and Co2+, *Science*, 2008, *321*, 1072-1075
[40] Risch, M., Klingan, K., Ringleb, F., Chernev, P., Zaharieva, I., Fischer, A., Dau, H., Water Oxidation by Electrodeposited Cobalt Oxides—Role of Anions and Redox-Inert Cations in Structure and Function of the Amorphous Catalyst, *ChemSusChem*, 2012, *5*, 542-549
[41] Klingan, K., Ringleb, F., Zaharieva, I., Heidkamp, J., Chernev, P., Gonzalez-Flores, D., Risch, M., Fischer, A., Dau, H., Water Oxidation by Amorphous Cobalt-Based Oxides: Volume Activity and Proton Transfer to Electrolyte Bases, *ChemSusChem*, 2014, *7*, 1301-1310
[42] Amin, H. M. A., Königshoven, P., Hegemann, M., Baltruschat, H., Role of Lattice Oxygen in the Oxygen Evolution Reaction on Co3O4: Isotope Exchange Determined Using a Small-Volume Differential Electrochemical Mass Spectrometry Cell Design, *Analytical Chemistry*, 2019, *91*, 12653-12660
[43] Kanan, M. W., Yano, J., Surendranath, Y., Dincă, M., Yachandra, V. K., Nocera, D. G., Structure and Valency of a Cobalt−Phosphate Water Oxidation Catalyst Determined by in Situ X-ray Spectroscopy, *Journal of the American Chemical Society*, 2010, *132*, 13692-13701
[44] Gao, L., Cui, X., Sewell, C. D., Li, J., Lin, Z., Recent advances in activating surface reconstruction for the high-efficiency oxygen evolution reaction, *Chemical Society Reviews*, 2021, *50*, 8428-8469
[45] Wiegmann, T., Pacheco, I., Reikowski, F., Stettner, J., Qiu, C., Bouvier, M., Bertram, M., Faisal, F., Brummel, O., Libuda, J., Drnec, J., Allongue, P., Maroun, F., Magnussen, O. M., Operando Identification of the Reversible Skin Layer on Co3O4 as a Three-Dimensional Reaction Zone for Oxygen Evolution, *ACS Catalysis*, 2022, *12*, 3256-3268
[46] Faisal, F., Bertram, M., Stumm, C., Cherevko, S., Geiger, S., Kasian, O., Lykhach, Y., Lytken, O., Mayrhofer, K. J. J., Brummel, O., Libuda, J., Atomically Defined Co3O4(111) Thin Films Prepared in

Ultrahigh Vacuum: Stability under Electrochemical Conditions, *The Journal of Physical Chemistry C*, 2018, *122*, 7236-7248
[47] Faisal, F., Stumm, C., Bertram, M., Waidhas, F., Lykhach, Y., Cherevko, S., Xiang, F., Ammon, M., Vorokhta, M., Šmíd, B., Skála, T., Tsud, N., Neitzel, A., Beranová, K., Prince, K. C., Geiger, S., Kasian, O., Wähler, T., Schuster, R., Schneider, M. A., Matolín, V., Mayrhofer, K. J. J., Brummel, O., Libuda, J., Electrifying model catalysts for understanding electrocatalytic reactions in liquid electrolytes, *Nature Materials*, 2018, *17*, 592-598
[48] Fester, J., Makoveev, A., Grumelli, D., Gutzler, R., Sun, Z., Rodríguez-Fernández, J., Kern, K., Lauritsen, J. V., The Structure of the Cobalt Oxide/Au Catalyst Interface in Electrochemical Water Splitting, *Angewandte Chemie International Edition*, 2018, *57*, 11893-11897
[49] Pacheco, I., Bouvier, M., Magnussen, O. M., Allongue, P., Maroun, F., Growth of Ultrathin Well-Defined and Crystalline Films of Co3O4 and CoOOH by Electrodeposition, *JOURNAL OF THE ELECTROCHEMICAL SOCIETY*, 2023, *170*, 012501
[50] Stoerzinger, K. A., Choi, W. S., Jeen, H., Lee, H. N., Shao-Horn, Y., Role of Strain and Conductivity in Oxygen Electrocatalysis on LaCoO3 Thin Films, *The Journal of Physical Chemistry Letters*, 2015, *6*, 487-492
[51] Jeen, H., Bi, Z., Choi, W. S., Chisholm, M. F., Bridges, C. A., Paranthaman, M. P., Lee, H. N., Orienting Oxygen Vacancies for Fast Catalytic Reaction, *Advanced Materials*, 2013, *25*, 6459-6463
[52] Weber, M. L., Baeumer, C., Mueller, D. N., Jin, L., Jia, C.-L., Bick, D. S., Waser, R., Dittmann, R., Valov, I., Gunkel, F., Electrolysis of Water at Atomically Tailored Epitaxial Cobaltite Surfaces, *Chemistry of Materials*, 2019, *31*, 2337-2346
[53] Seitz, L. C., Dickens, C. F., Nishio, K., Hikita, Y., Montoya, J., Doyle, A., Kirk, C., Vojvodic, A., Hwang, H. Y., Norskov, J. K., Jaramillo, T. F., A highly active and stable IrOx/SrIrO3 catalyst for the oxygen evolution reaction, *Science*, 2016, *353*, 1011-1014
[54] Ravel, B., Newville, M., ATHENA, ARTEMIS, HEPHAESTUS: data analysis for X-ray absorption spectroscopy using IFEFFIT, *Journal of Synchrotron Radiation*, 2005, *12*, 537-541
[55] Dau, H., Liebisch, P., Haumann, M., X-ray absorption spectroscopy to analyze nuclear geometry and electronic structure of biological metal centers—potential and questions examined with special focus on the tetra-nuclear manganese complex of oxygenic photosynthesis, *Anal Bioanal Chem*, 2003, *376*, 562-583
[56] Timoshenko, J., Roldan Cuenya, B., In Situ/Operando Electrocatalyst Characterization by X-ray Absorption Spectroscopy, *Chemical Reviews*, 2021, *121*, 882-961
[57] Pasquini, C., Liu, S., Chernev, P., Gonzalez-Flores, D., Mohammadi, M. R., Kubella, P., Jiang, S., Loos, S., Klingan, K., Sikolenko, V., Mebs, S., Haumann, M., Beyer, P., D'Amario, L., Smith, R. D. L., Zaharieva, I., Dau, H., Operando tracking of oxidation-state changes by coupling electrochemistry with time-resolved X-ray absorption spectroscopy demonstrated for water oxidation by a cobalt-based catalyst film, *Anal Bioanal Chem*, 2021, *413*, 5395-5408
[58] Chen, H.-Y., Chang, Y.-C., Lee, J.-F., Pao, C.-W., Huang, H.-C., Wang, C.-H., Operando Identification of Hydrangea-like and Amorphous Cobalt Oxyhydroxide Supported by Thin-Layer Copper for Oxygen Evolution Reaction, *ACS Sustainable Chemistry & Engineering*, 2021, *9*, 12300-12310
[59] Behl, W. K., Toni, J. E., Anodic oxidation of cobalt in potassium hydroxide electrolytes, *Journal of Electroanalytical Chemistry and Interfacial Electrochemistry*, 1971, *31*, 63-75
[60] Doyle, R. L., Godwin, I. J., Brandon, M. P., Lyons, M. E. G., Redox and electrochemical water splitting catalytic properties of hydrated metal oxide modified electrodes, *Physical Chemistry Chemical Physics*, 2013, *15*, 13737-13783
[61] Koza, J. A., He, Z., Miller, A. S., Switzer, J. A., Electrodeposition of Crystalline Co3O4—A Catalyst for the Oxygen Evolution Reaction, *Chemistry of Materials*, 2012, *24*, 3567-3573
[62] Pasquini, C., Liu, S., Chernev, P., Gonzalez-Flores, D., Mohammadi, M. R., Kubella, P., Jiang, S., Loos, S., Klingan, K., Sikolenko, V., Mebs, S., Haumann, M., Beyer, P., D'Amario, L., Smith, R. D. L., Zaharieva, I., Dau, H., Operando tracking of oxidation-state changes by coupling electrochemistry

with time-resolved X-ray absorption spectroscopy demonstrated for water oxidation by a cobalt-based catalyst film, *Anal Bioanal Chem*, 2021, *413*, 5395-5408
[63] Creazzo, F., Oxygen evolution reaction at cobalt oxides/water interfaces: heterogeneous electrocatalysis by DFT-MD simulations & metadynamics, in, Université Paris-Saclay, 2020,